The Effects of VIIRS Detector-Level and Band-Averaged Relative Spectral Response Differences Between S-NPP and NOAA-20 on the Thermal Emissive Bands

Lin Lin and Changyong Cao

***Abstract*—The Joint Polar Satellite System-1 (renamed NOAA-20 after reaching the polar orbit) was successfully launched on November 18, 2017, into an afternoon orbit with a local equator crossing time of ∼1:30 P.M., in the same orbital plane as the Suomi National Polar-orbiting Partnership (S-NPP) but with a time separation of 50 min. The NOAA-20 Visible Infrared Imaging Radiometer Suite (VIIRS) will become the primary operational imager succeeding the VIIRS onboard S-NPP, which has been in orbit for more than six years. Although the VIIRS onboard S-NPP and NOAA-20 have identical designs, there are small differences in the relative spectral response (RSR) in most bands. Previous studies have shown that minor differences in the S-NPP RSRs at thermal emissive bands (TEBs) can lead to several effects at the detector level, such as striping in sensor data record (SDR) products. Such differences may explain the striping pattern found in S-NPP VIIRS sea surface temperature (SST) products. This article analyzes the detector-level and operational band-averaged RSRs for NOAA-20 VIIRS TEBs and examines the radiometric response to them using the line-by-line radiative transfer model at a very high spectral resolution for convolving with the RSRs. We also evaluate the impact of RSR differences between S-NPP and NOAA-20 for radiometric biases and potential striping in VIIRS TEB SDR brightness temperature. This article will contribute toward measurement consistency for long-term observations in the thermal infrared bands and ensure the quality of retrieval data produced by VIIRS, such as SST, fire, and other retrievals.**

***Index Terms*—Line-by-line radiative transfer model (LBLRTM), relative spectral response (RSR), sensor data record (SDR) product, thermal emissive band (TEB), Visible Infrared Imaging Radiometer Suite (VIIRS).**

I. Introduction

ON NOVEMBER 18, 2017, the Joint Polar Satellite System-1 satellite was successfully launched into an orbit with an inclination angle of 98.7° to the equator and 824 km above the earth, joining the Suomi National Polar-orbiting Partnership (S-NPP) satellite in the same orbit with a separation of half an orbit or ∼50 min. Onboard both NOAA-20 and S-NPP satellites is the Visible Infrared Imaging Radiometer Suite (VIIRS), which is a scanning imaging radiometer that produces global imagery and radiometric measurements of the land, atmosphere, cryosphere, and oceans in the visible and infrared bands with moderate spatial resolutions. VIIRS has 22 spectral bands, covering the wavelengths from 0.4 to 11.8 μm, including 14 reflective solar bands (RSBs), seven thermal emissive bands (TEBs), and one day–night band (DNB). At the VIIRS focal plane, each moderate-resolution (M) band has 16 detectors aligned in the along-track direction, and as the rotating telescope assembly scans the earth, these detectors sweep out a swath from scan angle -56.28^{o} to $+56.28^{o}$ [1]. A striping pattern in the imagery of the measured brightness temperature occurs along the track as a side effect of such a multidetector arrangement. Tables I–III summarize general information and calibration specifications (spec) along with the on-orbit signal-to-noise ratio (SNR), noise equivalent ΔT (NEDT) performances of the NOAA-20 VIIRS and S-NPP bands.

Since launch, the ground interface data and processing segment (IDPS) has processed NOAA-20 VIIRS data including calibration, geolocation, telemetry, and housekeeping. The raw data processing software, which employs the radiometric calibration algorithm, converts raw digital numbers from earth view (EV) observations into various sensor data record (SDR) radiance products. NOAA-20 VIIRS SDR data were declared at the beta maturity level on January 25, 2018, the provisional maturity level on February 19, 2018, and the validated maturity level on June 15, 2018, after intensive evaluations of the instrument performance and significant improvements in the radiometric and geometric accuracies. Radiometrically calibrated, earth-located, and spectrally defined data from one or more VIIRS bands, SDRs are used as input to retrieve VIIRS Environmental Data Record (EDR) products. VIIRS provides over 20 EDR products, including snow/ice cover, clouds, fog, aerosols, fire, smoke plumes, vegetation health, and phytoplankton abundance/chlorophyll. The NOAA JSTAR website provides the maturity level status of these products (https://www.star.nesdis.noaa.gov/jpss/

Manuscript received September 12, 2018; revised May 6, 2019 and June 26, 2019; accepted August 26, 2019. Date of publication September 23, 2019; date of current version November 22, 2019. This work was supported by NOAA Grant NA14NES4320003 (Cooperative Institute for Climate and Satellites) at the University of Maryland/ESSIC. This paper was presented in part at the IEEE 2018 International Geoscience and Remote Sensing Symposium, Valencia, Spain, September 15, 2018. *(Corresponding author: Lin Lin.)*

L. Lin is with the Cooperative Institute for Climate and Satellites, Earth System Science Interdisciplinary Center, University of Maryland, College Park, MD 20740 USA (e-mail: linlin@umd.edu).

C. Cao is with the NOAA Center for Satellite Applications and Research, College Park, MD 20740 USA (e-mail: changyong.cao@noaa.gov).

Color versions of one or more of the figures in this article are available online at http://ieeexplore.ieee.org.

Digital Object Identifier 10.1109/JSTARS.2019.2938221

TABLE I
REQUIREMENTS AND CHARACTERISTICS OF VIIRS RSBS

Band	Spectral Range (μm)	L_{typ}* $W/(m^2 \cdot sr \cdot \mu m)$	SNR#		
			Spec	NOAA-20	S-NPP
M1	0.402-0.422	HG$: 155	316	1115	1045
		LG&: 44.9	352	644	588
M2	0.436-0.454	HG: 146	409	1012	1010
		LG: 40	380	573	572
M3	0.478-0.498	HG: 123	414	1057	988
		LG: 32	416	686	628
M4	0.545-0.565	HG: 90	315	857	856
		LG:21	362	551	534
M5	0.662-0.682	HG: 68	360	762	631
		LG: 10	242	383	336
M6	0.739-0.754	9.6	199	413	368
M7	0.846-0.885	HG: 33.4	340	708	631
		LG: 6.4	215	523	457
M8	1.230-1.250	5.4	74	319	221
M9	1.371-1.386	6	83	297	227
M10	1.580-1.640	7.3	342	653	586
M11	2.225-2.275	1	90	198	22**
I1	0.600-0.680	22	119	224	214
I2	0.846-0.885	25	150	285	264
I3	1.580-1.640	7.3	6	174	149

*$L_{\rm typ}$: Typical calibration spectral radiance in $W/(m^2 \cdot sr \cdot \mu m)$**For S-NPP M11, $L_{\rm typ} = 0.12\ W/(m^2 \cdot sr \cdot \mu m)$ #SNR: Unitless $HG: High Gain &LG: Low Gain.

TABLE II
REQUIREMENTS AND CHARACTERISTICS OF VIIRS TEBS

Band	Spectral Range (μm)	T_{typ}* (K)	NEDT (K)		
			Spec	NOAA-20	S-NPP
M12	3.660-3.840	270	0.396	0.12	0.12
M13	3.973-4.128	300	0.107	0.04	0.04
M14	8.400-8.700	270	0.091	0.05	0.06
M15	10.263-11.263	300	0.07	0.02	0.03
M16	11.538-12.488	300	0.072	0.03	0.03
I4	3.550-3.930	270	2.5	0.42	0.4
I5	10.500-12.400	210	1.5	0.42	0.4

*$T_{\rm typ}$: Typical calibration temperature in K.

TABLE III
REQUIREMENTS AND CHARACTERISTICS OF VIIRS DNB

Band	Spectral Range (μm)	L_{min}*	SNR		
			Spec	NOAA-20	S-NPP
DNB	0.500-0.900	3	6	>10	>10

*$L_{\rm min}$: Minimum spectral radiance required to meet calibration specification in $W/(m^2 \cdot sr \cdot \mu m)$.

AlgorithmMaturity.php). VIIRS SDR and EDR products have been distributed to the user community from NOAA's comprehensive large array-data stewardship systems (CLASS) for various applications, such as monitoring hurricane/typhoons, and measuring cloud and aerosol properties, ocean color, sea and land surface temperatures, ice motion and temperature, active fires, and Earth's albedo.

The VIIRS detector-level relative spectral response (RSR) is measured during prelaunch testing. However, for simplification and computational efficiency, the IDPS uses the band-averaged RSR, i.e., the average of all detector-level RSRs [2]. Previous studies [3], [4] have compared the detector-level and band-averaged RSRs of the S-NPP TEB M15 (10.7 μm) and M16 (11.8 μm) bands and evaluated the effects of the detector-level spectral response on striping in the TEB SDRs. Small differences in the detector-level RSR tends to lead to striping in SDRs. For example, S-NPP VIIRS level-2 sea surface temperature (SST) retrievals show a clear striping pattern. Such a striping pattern would degrade the quality of the SST retrieval and would also deteriorate the performance of the VIIRS cloud mask product.

In this article, we examine the effects of the detector-level and band-averaged RSRs on NOAA-20 VIIRS TEBs. We also assess in detail the impact of the spectral response differences between S-NPP and NOAA-20 on VIIRS TEBs using radiative transfer model simulations and SDR brightness temperature products. Section II introduces the methodology used to simulate VIIRS TEB radiances/brightness temperatures using a radiative transfer model. Section III compares the model-simulated TEB radiances/brightness temperatures from S-NPP and NOAA-20 band-averaged RSRs. Section IV presents the impact of detector-level and band-averaged RSR differences on NOAA-20 VIIRS TEB simulations. Section V discusses the effects of detector-level RSRs on S-NPP and NOAA-20 VIIRS SDR striping. Section VI gives a summary and conclusions.

II. METHODOLOGY FOR SIMULATING VIIRS TEB RADIANCES USING THE LINE-BY-LINE RADIATIVE TRANSFER MODEL (LBLRTM)

In this article, the LBLRTM developed by Atmospheric and Environmental Research, Inc., is used to simulate VIIRS TEB radiances. The LBLRTM is an accurate and flexible radiative transfer model covering the full spectrum from the microwave to the ultraviolet [5]–[7]. It employs the Voigt line shape at all atmospheric levels, the self- and foreign-broadened water vapor continuum model, the MT_CKDwater vapor continuum absorption model [8]–[10], and HITRAN line database parameters [11]–[14]. High-resolution spectral measurements from the ground [9], [15] and from satellite [16]–[18] have validated the LBLRTM, and calculations in the thermal infrared region are a reference standard for intercomparisons of radiative transfer models. Moreover, it has been widely used as the foundation for retrieval algorithms and to train fast RTMs (such as the community radiative transfer model) employed in numerical weather prediction data assimilation systems [7]. More details about the LBLRTM including recent updates have been summarized by others [6], [7].

To represent the range of variations in temperature, water vapor, and absorber amount in the real atmosphere, six representative atmospheric conditions in the LBLRTM (tropical, mid-latitude summer, mid-latitude winter, sub-arctic summer, sub-arctic winter, and the 1976 U.S. standard atmosphere) are used to perform VIIRS TEB simulations. For simplicity, simulations were carried out under clear-sky conditions, and the surface

was set to be an ocean surface with temperatures of 300, 290, 273, 280, 263, and 290 K for the six atmospheres, respectively.

The latest version of LBLRTM V12.8 released in August 2017 is used to simulate the top-of-the-atmosphere (TOA) radiance at a spectral resolution of 0.01 cm^{-1} for VIIRS TEBs. Because the output of the LBLRTM is in wavenumber (ν) space, the measured detector-level and band-averaged RSRs in wavelength space $r(\lambda)$ are converted to wavenumber space $r(\nu)$ first. A linear interpolation in wavenumber is then carried out to ensure an even wavenumber sampling. After that, the LBLRTM output TOA spectral radiance $R(\nu)$ at wavenumber ν is convolved with the RSR $r(\nu)$ (either detector level or band averaged) to obtain the in-band mean effective radiance $\overline{R}$ as follows:

$$\overline{R} = \frac{\int_{\nu_1}^{\nu_2} r(\nu) \cdot R(\nu) d\nu}{\int_{v_1}^{v_2} r(\nu) d\nu}. \quad (1)$$

The effective brightness temperature (T_b) is then converted from $\overline{R}$ using precalculated VIIRS-radiance to brightness-temperature conversion look-up tables (LUTs). The original VIIRS LUTs [19] provide the conversion of radiance in wavelength units to temperature. However, the spectral radiance output from the LBLRTM is in wavenumber units. We therefore computed the spectral radiance $L(\nu, T)$ of wavenumber ν (unit: cm^{-1}) at the (blackbody) temperature T (unit: K) in the original VIIRS LUT using the Planck function according to

$$L(\nu, T) = \frac{c_1 \nu^3}{e^{\frac{c_2 \nu}{T}} - 1} \quad (2)$$

where $c_1 = 1.191042 \times 10^8 \quad W/(m^2 \cdot sr \cdot ctextm^{-1})$, and $c_2 = 1.4387752$ K $\cdot$ cm. Detector-level and band-averaged effective brightness temperatures, i.e., T_b (det RSR) and T_b (avg RSR), respectively, can be converted from radiances using their corresponding LUTs. The difference between T_b(det RSR)and T_b(avg RSR) will be investigated to assess the impact of detector-level RSR differences on striping, possible atmospheric dependence, and detector stability in the following section.

III. Differences in VIIRS TEB Band-Averaged RSRs Between NOAA-20 and S-NPP

VIIRS is a whiskbroom scanning radiometer with a scan angle range of 112.56° at a nominal altitude of 829 km. It has many detectors with slightly different RSRs. The band-averaged RSR is the average of all detector RSRs within a given band, determined through measurements made during prelaunch testing. Although VIIRS detector-level RSRs are available, VIIRS SDR brightness temperature retrievals are derived from radiance data using the band-averaged RSR for each band by IDPS to simplify processing and optimize computational efficiency.

The detector-level and band-averaged RSRs for S-NPP and NOAA-20 are available at the STAR JPSS website (https://www.star.nesdis.noaa.gov/jpss/VIIRS.php). The S-NPP VIIRS RSRs have been measured multiple times and independently analyzed by both the Northrop Grumman and Government teams. In this article, we chose the S-NPP RSR from instrument-level testing version 1.0 published in April 2013 (https://ncc.nesdis.noaa.gov/VIIRS/VIIRSSpectralResponseFunctions.php) and the NOAA-20 RSR published in November 2016 (https://ncc.nesdis.noaa.gov/NOAA-20/J1VIIRS_NOAA20_SpectralResponseFunctions.php). The spectral sample interval of the RSRs for bands M12, M13, M14, M15, and M16 (band M16 includes two detector arrays A and B, which are time-delay integrated) is at 0.0065, 0.0075, 0.02, 0.05, and 0.06 μm, respectively. Fig. 1 shows the band-averaged RSRs of VIIRS TEBs M12-M16 for S-NPP and NOAA-20. Except for M14, the S-NPP and NOAA-20 band-averaged RSRs differ. This may lead to radiometric biases between S-NPP and NOAA-20.

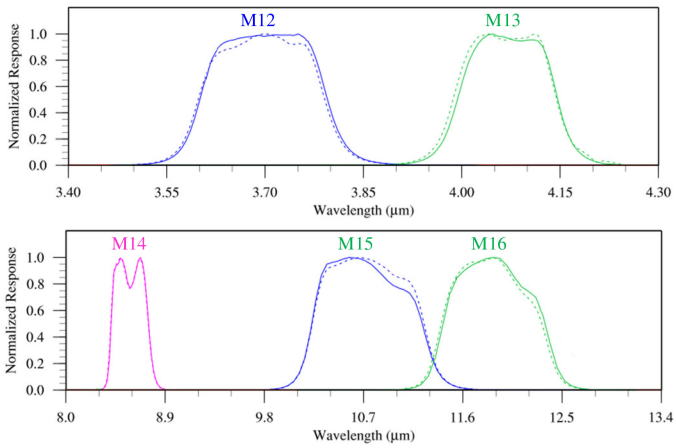

Fig. 1. Band-averaged RSRs for VIIRS TEBs M12−M16 on S-NPP (dotted lines) and NOAA-20 (solid lines).

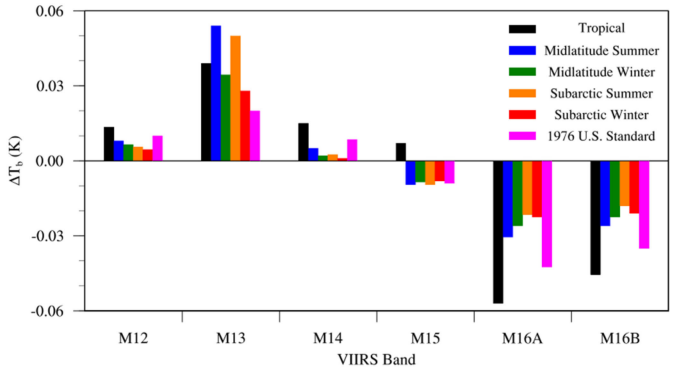

Fig. 2. Effective brightness temperature differences between using NOAA-20 and S-NPP band-averaged RSRs ($T_b^{NOAA-20} - T_b^{S-NPP}$) in VIIRS TEBs M12-M16 from LBLRTM simulations for six representative atmospheres.

Fig. 2 provides a summary of the magnitudes of the T_b differences resulting from the use of S-NPP and NOAA-20 VIIRS TEB band-averaged RSRs from LBLRTM output for six atmospheres. The magnitudes in M13 and M16 for all atmospheric conditions are larger than in other bands (>0.02 K). The magnitudes of the differences depend on the atmospheric condition: tropical and mid-latitude cases generally have a larger magnitude than the subarctic case, except for the subarctic summer case for M13. In general, the T_b differences show a dependence on the atmospheric condition although the magnitudes of the differences are less than 0.06 K. When generating long-term

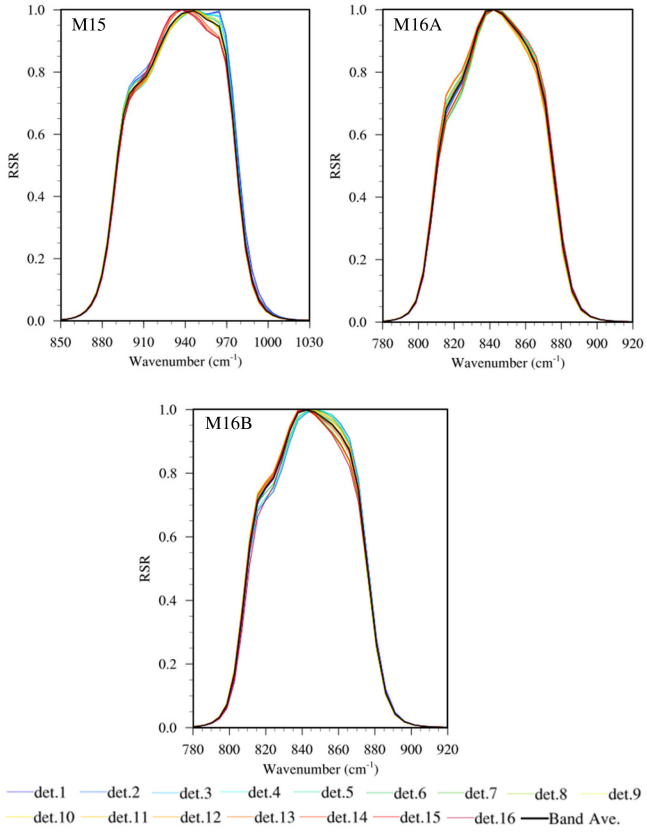

Fig. 3. Sixteen detector-level (color-coded) and band-averaged (black) RSRs of NOAA-20 VIIRS M15, M16A, and M16B.

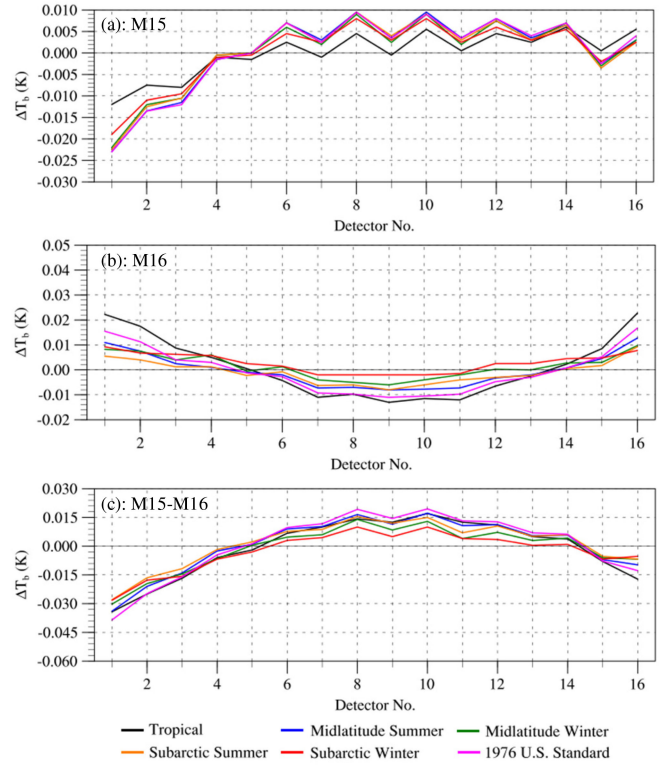

Fig. 4. Effective brightness temperature difference between detector-level and band-averaged RSRs ($\Delta T_b = T_b(\det\ RSR) - T_b(\text{avg}\ RSR)$) for six representative atmospheres in NOAA-20 VIIRS TEB. (a) M15. (b) M16. (c) Difference M15−M16.

consistent VIIRS TEB observations, careful consideration of the radiometric biases of NOAA-20 and S-NPP is needed.

IV. Differences Between Detector-Level and Band-Averaged RSRs for NOAA-20 and S-NPP From LBLRTM Simulations

In this section, we analyze the possibility of striping caused by the difference in the effective brightness temperature (ΔT_b) between the detector-level and band-averaged RSRs, expressed as

$$\Delta T_b = T_b(\det\ RSR) - T_b(\text{avg}\ RSR) \tag{3}$$

where $T_b(\det\ RSR)$and $T_b(avg\ \text{RSR})$are the T_b computed using detector-level and band-averaged RSRs, respectively, (see Section II).

Fig. 3 shows the detector-level and band-averaged RSR functions for NOAA-20 VIIRS M15, M16A, and M16B [1]. The NOAA-20 RSRs are slightly different among the detectors because of the staggered detector layout of each channel's detectors on the focal plane array. This induces small optical path differences between detectors not accounted for by the band-averaged RSR for each channel [20]. Such differences are expected to affect in-band radiances and hence T_b. Fig. 4 shows the impact of this detector-level variation on imagery artifacts.

Fig. 4(a) for NOAA-20 M15 shows a clear atmospheric dependence. An odd/even detector pattern due to the staged detector layout on the focal plan [20] is also observed. The smallest brightness temperature difference ΔT_b is at detector 4 (the difference is close to zero), meaning that this detector matches the band-averaged RSR best. The magnitude of the variation is 0.018 K for the tropical atmosphere, and 0.033 K for the subarctic atmosphere. Detectors 1 and 2 deviate most from the band-averaged RSR than other detectors. The $T_b$for detectors 1–3, 5, and 15 are smaller than the band-averaged value, but the T_b for detectors 6–14 and 16 are larger than the band-averaged value.

M16 is the average of M16A and M16B [Fig. 4(b)]. There is a more obvious atmospheric impact on the M16 ΔT_b. In contrast to M15 [Fig. 4(a)], the tropical atmosphere has the largest variation, with a magnitude of 0.036 K, and the subarctic atmosphere ΔT_b variation is 0.012 K. Detectors 1, 2, and 16 deviate more from the band-averaged RSR than other detectors. Detectors 5 and 14 match the band-averaged RSR better. The odd/even detector pattern is not as obvious as in M15. Fig. 4(b) also shows that in the M16 band, T_b for detectors 1–5 and 14–16 are larger than the band-averaged value, but T_b for detectors 6–13 are smaller than the band-averaged value.

The differences in observed T_b between M15 and M16 ($T_{b,M15} - T_{b,M16}$) are used in level 2 VIIRS SST EDR retrievals [3], [21], [22]. This technique tends to magnify $T_{b,M15} - T_{b,M16}$ by roughly a factor of 3–4, which in turn can amplify system artifacts and propagate into the SST products [21], [22]. Therefore, the difference between detector-level and

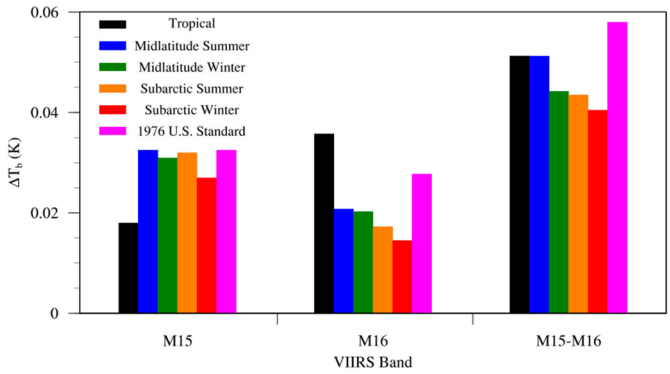

Fig. 5. Magnitude of brightness temperature difference ΔT_b between using detector-level and band-averaged RSR for six atmospheric conditions.

band-averaged brightness temperatures $T_{b,M15} - T_{b,M16}$ is also analyzed [Fig. 4(c)]. The T_b for detectors 1–5, 15, and 16 are smaller than the band-averaged value, but the T_b for detectors 6–14 are larger than the band-averaged value. There is also an atmospheric dependence, with the magnitude of the variation in $T_{b,M15} - T_{b,M16}$ equal to 0.041 K for the tropical atmosphere and 0.04 K for the subarctic. In other words, the atmospheric impact is more obvious in the band difference $T_{b,M15} - T_{b,M16}$ [Fig. 4(c)] than for a single band [Fig. 4(a) and (b)]. VIIRS Earth observation data are further analyzed in Section V to examine whether there are a systematic atmospheric dependence and detector stability in operational VIIRS SDR radiance products.

Fig. 5 provides a summary of the magnitudes of the T_b differences resulting from the use of detector-level and band-averaged NOAA-20 RSRs from LBLRTM output for six atmospheres, i.e., the maximum variation in ΔT_b for all 16 detectors shown in Fig. 4. The magnitude of $T_{b,M15} - T_{b,M16}$ is larger than that in a single band. Comparing M16 and $T_{b,M15} - T_{b,M16}$, M15 is much less atmospheric-state dependent. Except for M15 and the standard atmosphere case, the magnitude has a clear atmospheric dependence, i.e., the tropical case has a much larger magnitude than the subarctic cases.

In general, the results from LBLRTM simulations suggest that atmospheric dependence exists although the magnitude of ΔT_b between detector-level and band-averaged RSR for different atmospheric conditions is less than 0.06 K. Water vapor also has an impact on the striping pattern seen in satellite images. For example, in M16, the variance of ΔT_b between using the detector-level and band-averaged RSRs is the largest for the tropical case and the smallest for the subarctic winter case. That is, a warm and moist atmosphere has a larger atmospheric impact on ΔT_b than a cold and dry atmosphere. The atmospheric impact is more obvious in the band difference $T_{b,M15} - T_{b,M16}$ than for a single band. The variances of ΔT_b for the tropical and subarctic atmospheres are 0.041 and 0.04 K in $T_{b,M15} - T_{b,M16}$, and 0.036 and 0.012 K in M16, respectively. Compared to the band-averaged situation, detectors 1–3 show larger atmospheric effects, with detector 1 showing the largest difference up to 0.041 K for the optical case. This suggests that these detectors are more sensitive to gain instability than the other detectors due to the inherent artifacts induced by the detector-level RSR differences.

Compared with the assessment of the effects of the S-NPP VIIRS M15/M16 detector radiometric stability and RSR variations in striping [3], [4] (figures omitted), there are some similarities and slight differences between NOAA-20 VIIRS M15/M16. For both S-NPP and NOAA-20, detectors 1 and 2 deviate most from the band average than other detectors at M15/M16. The atmospheric impact on the T_b difference in M16 is stronger than that in M15, and the tropical atmosphere case has the largest variation. Apparent odd/even detector patterns are noticeable as well. At M16, the T_b for detectors 1–5 are larger than the band-averaged value, but the T_b for detectors 6 and 8–16 are smaller than the band-averaged value. However, for S-NPP, the smallest T_b difference for M15 is at detector 5 (not detector 4 as for NOAA-20). The magnitudes of the variations caused by the detector-level RSR are smaller for S-NPP M15 (0.01 K for the tropical atmosphere and 0.025 K for the subarctic atmosphere) and larger for S-NPP M16 (0.063 K for tropical atmosphere and 0.022 K for subarctic atmosphere) and $T_{b,M15} - T_{b,M16}$ (0.071 K for the tropical atmosphere and 0.048 K for the subarctic atmosphere). Also, S-NPP VIIRS M15 and M16 ΔT_b are negative at detectors 15 and 16 and positive at detector 1, leading to a larger ΔT_b between detectors 16 and 1, and therefore a larger brightness temperature difference $T_{b,M15} - T_{b,M16}$ between detectors 16 and 1. The difference between M15 and M16 is smaller for NOAA-20 ($\sim$0.055 K) than for S-NPP ($\sim$0.07 K). The striping in the NOAA-20 TEB SDRs is thus expected to be $\sim$20% less than that in the S-NPP TEB SDRs, which may also be reflected in the SST retrievals.

V. Striping Patterns in NOAA-20 and S-NPP VIIRS TEB SDRs

The operational IDPS uses band-averaged RSRs to derive SDR T_b products, under the assumption that the detector-level RSRs for a given band are not significantly different from the band-averaged RSR. The LBLRTM simulations presented in Section IV demonstrated that there is a noticeable impact of the detector-level and band-averaged RSR differences on the TEBs. In this section, a sample of operational NOAA-20 VIIRS T_b data for bands M15 and M16 are analyzed to examine the existence of the striping pattern in SDR radiance products.

The sample shows a clear-sky "uniform" open ocean surface near the Bay of Bengal on April 21, 2018 (Fig. 6). It has the size of 62 pixels along the scan direction and 16 scans $\times$ 16 detectors in the along-track direction.

Fig. 7 was produced by taking the average of each detector (along the scan direction of 62 pixels) for each of the 16 scans and then averaging the scan averages on a per detector basis to assess if the systematic detector-level patterns in Section IV are seen in this sample case. There is a general sloped structure from detector 1–16 in M15 and M16 [Fig. 7(a) and (b)] and an arc-like pattern across the detectors in M15−M16 [Fig. 7(c)]. There is also a clear detector-to-detector odd/even pattern in the M16 data, though more evident in the M15 data with absolute average detector-to-detector differences at the noise level of $\sim$0.02 and $\sim$0.01 K for M15 and M16, respectively. As discussed previously, the M15−M16 difference plays a critical role in the

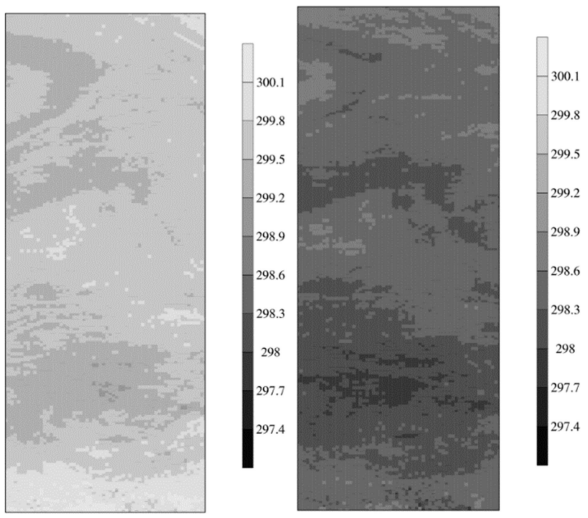

Fig. 6. NOAA-20 VIIRS SDR M15 (left panel) and M16 (right panel) brightness temperatures (unit: K) of the clear-sky open ocean near the Bay of Bengal on April 21, 2018.

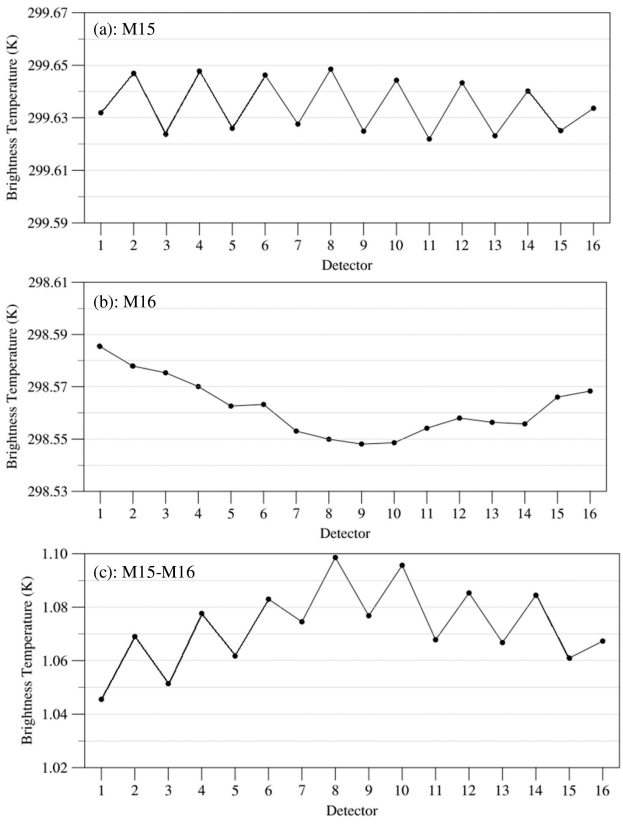

Fig. 7. Detector-averaged brightness temperatures at (a) M15, (b) M16, and (c) M15−M16, using the data shown in Fig. 6.

VIIRS SST retrieval product. Fig. 7(c) shows that the magnitudes of the detector-to-detector differences are slightly larger for $T_{b,M15} - T_{b,M16}$ (∼0.022 K) compared with the differences in M15 and M16 [Fig. 7(a) and (b)]. These findings from operational SDR products are consistent with the LBLRTM simulations discussed in Section IV and emphasize the need

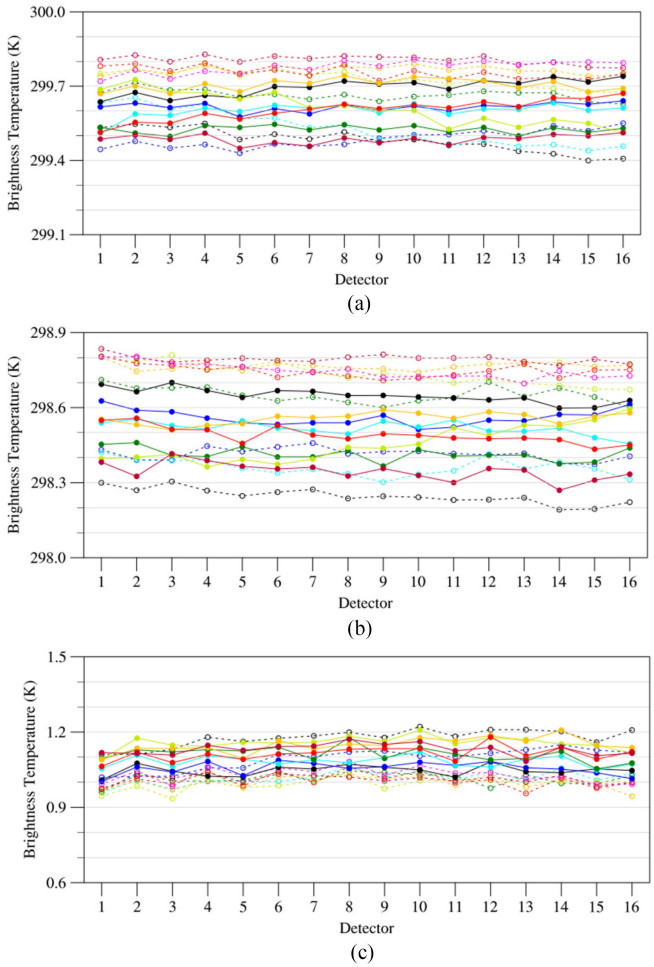

Fig. 8. Averaged detector-level data (across 62 pixels along the scan direction) as a function of scan for (a) M15, (b) M16, and (c) M15−M16.

for detector-level processing in both SDR and EDR products when users seek the optimal radiometric performance of VIIRS TEBs.

The scan-averaging techniques used to produce Fig. 7 tend to lose information about detector variability on a scan-to-scan basis within the 16 scans. To gain insight into the scan-to-scan detector-level variability, the 16-scan subset data shown in Fig. 6 were averaged across 62 pixels along the scan direction for each detector (Fig. 8). This was done to reduce noise and possible scene variations to investigate whether there is a systematic pattern in the detector-level data. The differences in scans are larger for M16 than M15, and $T_{b,M15} - T_{b,M16}$ is smaller than both M15 and M16. It is admittedly difficult to distinguish a clear systematic pattern in this limited test case.

To compare striping patterns, S-NPP VIIRS M15/M16 SDR data from a clear-sky open ocean surface near the Bay of Bengal on April 21, 2018, were examined as well. The domain also has the size of 62 pixels along the scan direction, and 16 scans × 16 detectors in the along-track direction (figures omitted). Similar to the T_b for NOAA-20 M15 and M16, there is a sloped structure from higher to lower $T_b$for detectors 1–16 [Figs. 8(a) and (b) and 9(a) and (b)]. The odd/even pattern is not apparent in

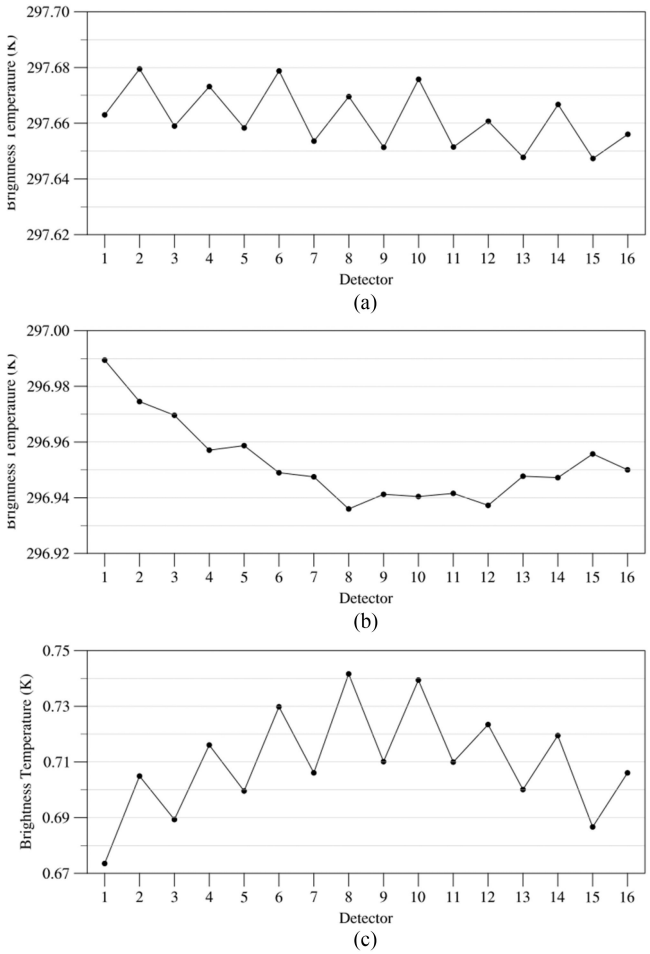

Fig. 9. Same as Fig. 7 except for using S-NPP brightness temperature products at (a) M15, (b) M16, and (c) M15−M16 of the clear-sky open ocean near the Bay of Bengal on April 21, 2018.

M16 data, but more evident in M15 data with absolute average detector-to-detector differences. The variation is larger than that for NOAA-20 (0.025 and 0.015 K for M15 and M16, respectively). Also, compared to the differences in M15 and M16, the magnitude of the detector-to-detector differences is larger for $T_{b,M15} - T_{b,M16}$ [$\sim$0.03 K, Fig. 9(c)], which is also larger than that for NOAA-20 [Fig. 7(c)]. This result is consistent with the LBLRTM simulation results discussed in Section IV, i.e., the striping in the NOAA-20 TEBs tends to be 20% less than that in the S-NPP TEBs. Furthermore, the variations among scans are somewhat sporadic with larger magnitudes for S-NPP than for NOAA-20 (figures omitted).

VI. Conclusion

This article examines S-NPP and NOAA-20 detector-level and band-averaged RSRs and their impacts on the VIIRS TEBs using LBLRTM simulations and operational SDR products.

First, a gross check of band-averaged TEB RSRs shows a clear difference between S-NPP and NOAA-20. LBLRTM simulation results show that such differences lead to a radiometric bias of larger than 0.02 K in M13 and M16 for all six representative atmosphere cases. There is also an atmospheric dependence although the difference is less than 0.06 K.

Next, the impact of the slight differences between detector-level and band-averaged RSRs on NOAA-20 VIIRS TEBs are analyzed. Found are odd/even detector-to-detector patterns, and LBLRTM simulations show slight atmospheric dependencies, i.e., the T_b difference in the tropical atmosphere case is generally larger than that in the subarctic atmosphere case. The magnitudes of the differences between tropical and subarctic atmospheres are -0.015 K in M15, 0.024 K in M16, and -0.017 K in M15$-$M16. For both S-NPP and NOAA-20, of all the detectors, detectors 1 and 2 deviate the most from the band average at M15/M16. Detectors 4 and 5 match the band-averaged RSR better. The atmospheric impact on T_b differences is more obvious in M16 than that in M15, and the tropical atmosphere pattern has the largest variation. Because the differences in observed T_b between M15 and M16 are used in the level-2 VIIRS SST EDR retrieval, we examined $T_{b,M15} - T_{b,M16}$ as well. The striping $T_{b,M15} - T_{b,M16}$ is more apparent than that in single band M15 and M16.

In addition to the LBLRTM simulation analysis, we also performed a case study to examine the existence of striping in NOAA-20 VIIRS SDR $T_b$products over a "uniform" region near the Bay of Bengal. In general, VIIRS SDR T_b observations are more variable than the model output because EV data are complex with mixed noise and diverse signals. Results from NOAA-20 show that ΔT_b is $\sim$0.02 K in M15, $\sim$0.01 K in M16, and $\sim$0.022 K in $T_{b,M15} - T_{b,M16}$. Results from S-NPP are larger: $\sim$0.025 K in M15, $\sim$0.015 K in M16, and $\sim$0.03 K in $T_{b,M15} - T_{b,M16}$. These results and the LBLRTM simulation results are consistent.

Acknowledgment

The authors would like to thank the NOAA/STAR VIIRS SDR team members in general, and in particular, S. Uprety, B. Zhang, and W. Wang for their help. The views, opinions, and findings contained in this article are those of the authors and should not be construed as official positions, policy, or decisions of the NOAA or the U.S. Government. Operational data used in this article are available at no cost through the NOAA/STAR JPSS website and NOAA CLASS. Other data used for this article are available from the authors.

References

[1] N. Baker and H. Kilcoyne, "NOAA. Joint polar satellite system (JPSS) VIIRS radiometric calibration algorithm theoretical basis document," 2013. [Online]. Available: https://nsidc.org/sites/nsidc.org/files/technical-references/JPSS-ATBD-VIIRS-SDR-C.pdf

[2] C. Moeller, J. McIntire, T. Schwarting, D.Moyer, and J. Costa, "Suomi NPP VIIRS spectral characterization: Understanding multiple RSR releases," *Proc. SPIE*, vol. 8510, pp. 1–15, 2012.

[3] F. Padula and C. Cao, "Detector-level spectral characterization of the sumo national polar-orbiting partnership Visible Infrared Imaging Radiometer Suite long-wave infrared bands M15 and M16," *Appl. Opt.*, vol. 54, no. 16, pp. 5109–5116, 2015.

[4] Z. Wang and C. Cao, "Assessing the effects of Suomi NPP VIIRS M15/M16 detector radiometric stability and relative spectral response variation on striping," *Remote Sens*., vol. 8, no. 2, 2016, Art. no. 145.
[5] S. A. Clough, M. J. Iacono, and J.-L. Moncet, "Line-by-line calculation of atmospheric fluxes and cooling rates: Application to water vapor," *J. Geophys. Res.*, vol. 97, pp. 15761–15785, 1992.
[6] S. A. Clough *et al.*, "Atmospheric radiative transfer modeling: A summary of the AER codes, short communication," *J. Quant. Spectrosc. Radiat. Transf.*, vol. 91, pp. 233–244, 2005.
[7] M. J. Alvarado *et al.*, "Performance of the line-by-lie radiative transfer model (LBLRTM) for temperature, water vapor, and trace gas retrievals: Recent updates evaluated with IASI case studies," *Atmospheric Chem. Phys.*, vol. 13, pp. 6687–6711, 2013.
[8] E. J. Mlawer, V. H. Payne, J.-L. Moncet, J. S. Delamere, M. J. Alvarado, and D. D. Tobin, "Development and recent evaluation of the MT_CKD model of continuum absorption," *Phil. Trans. Roy. Soc.*, vol. 370, pp. 1–37, 2012.
[9] J. S. Delamere, S. A. Clough, V. H. Payne, E. J. Mlawer, D. D. Turner, and R. R. Gamache, "A far-infrared radiative closure study in the Arctic: Application to water vapor," *J. Geophys. Res.*, vol. 115, no. D17106, pp. 1–17, 2010.
[10] V. H. Payne, E. J. Mlawer, K. E. Cady-Pereira, and J.-L. Moncet, "Water vapor continuum absorption in the microwave," *IEEE Trans. Geosci. Remote Sens.*, vol. 49, no. 6, pp. 2194–2208, Jun. 2011.
[11] F. Oyafuso *et al.*, "High accuracy absorption coefficients for the orbiting carbon observatory-2 (OCO-2) mission: Validation of updated carbon dioxide cross-sections using atmospheric spectra absorption coefficients for the OCO-2 mission," *J. Quant. Spectrosc. Radiat. Transf.*, vol. 203, pp. 213–223, 2017.
[12] D. C. Benner *et al.*, "Line parameters including temperature dependences of air- and self-broadened line shapes of $^{12}C^{16}O_2$: 2.06 μm region," *J. Mol. Spectrosc.*, vol. 326, pp. 21–47, 2016.
[13] V. M. Devi *et al.*, "Line parameters including temperature dependences of self- and foreign-broadened line shapes of $^{12}C^{16}O_2$: 1.6 μm region," *J. Quant. Spectrosc. Radiat. Transf.*, vol. 177, pp. 117–144, 2016.
[14] B. J. Drouin *et al.*, "Multispectrum analysis of the oxygen A-band," *J. Quant. Spectrosc. Radiat. Transf.*, vol. 186, pp. 118–138, 2016.
[15] M. W. Shephard, A. Goldman, S. A. Clough, and E. J. Mlawer, "Spectroscopic improvements providing evidence of formic acid in AERI-LBLRTM validation spectra," *J. Quant. Spectrosc. Radiat. Transf.*, vol. 82, pp. 383–390, 2003.
[16] M. J. Alvarado *et al.*, "Impacts of updated spectroscopy on thermal infrared retrievals of methane evaluated with HIPPO data," *Atmospheric Meas. Techn.*, vol. 8, pp. 965–985, 2015.
[17] M. J. Alvarado *et al.*, "Performance of the line-by-line radiative transfer model (LBLRTM) for temperature, water vapor, and trace gas retrievals: Recent updates evaluated with IASI case studies," *Atmospheric Chem. Phys.*, vol. 13, pp. 6687–6711, 2013.
[18] M. W. Shephard, S. A. Clough, V. H. Payne, W. L. Smith, S. Kireev, and K. E. Cady-Pereira, "Performance of the line-by-line radiative transfer model (LBLRTM) for temperature and species retrievals: IASI case studies from JAIVEx," *Atmospheric Chem. Phys.*, vol. 9, pp. 7397–7417, 2009.
[19] National Aeronautics and Space Administration, "Joint Polar Satellite System (JPSS) Ground Project Code 474 474-00001-08-B0124," in *Joint Polar Satellite System (JPSS) Common Data Format Control Book – External (CDFCB-X) Volume VIII—Look Up Table Formats*, 2015. [Online]. Available: https://www.jpss.noaa.gov/sciencedocuments/sciencedocs/2015-06/474-00001-08_JPSS-CDFCB-X-Vol-VIII_0124D.pdf
[20] C. Cao *et al.*, "Suomi NPP VIIRS sensor data record verification, validation, and long-term performance monitoring," *J. Geophys. Res. Atmos.*, vol. 118, pp. 11664–11678, 2013.
[21] M. Bouali and A. Ignatov, "Adaptive reduction of striping for improved sea surface temperature imagery from Suomi national polar orbiting partnership (S-NPP) Visible Infrared Imaging Radiometer Suite (VIIRS)," *J. Atmospheric Ocean. Technol.*, vol. 31, pp. 150–163, 2014.
[22] R. Godin, "VIIRS sea surface temperature algorithm theoretical basis document (ATBD)," Goddard Space Flight Center Greenbelt, Greenbelt, MD, USA, 2013.

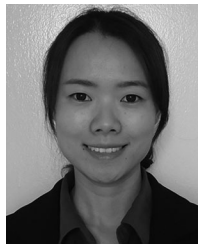

Lin Lin received the B.Sc. degree from the Nanjing University of Information Science and Technology, Nanjing, China, in 2002, and the master's and Ph.D. degrees in meteorology from Florida State University, Tallahassee, FL, USA, in 2005 and 2009, respectively.

She is currently with the Earth System Science Interdisciplinary Center, University of Maryland, College Park, MD, USA. Her primary research interests include calibration of satellite data at microwave wavelengths; intercalibration of satellite data using global positioning system radio occultation data; simulations of the microwave instrument using the community radiative transfer model, the monochromatic radiative transfer model, and line-by-line radiative transfer model; development of quality control techniques for improving uses of satellite data in numerical weather prediction models; direct assimilation of microwave radiances in the hurricane weather research and forecasting system; impact of direct assimilation of microwave radiances on hurricane forecasts; cloudy radiances through advanced radiative transfer models; cloud detection using the double-CO_2 band in the cross-track infrared sounder; and exploring the relationship between climate change and human science.

Changyong Cao received the Ph.D. degree in geography specializing in remote sensing and geographic information systems from Louisiana State University, Baton Rouge, LA, USA, in 1992.

He was an Assistant Professor and Laboratory Manager with Southern Illinois University in the early 1990s. Before joining National Oceanic and Atmospheric Administration (NOAA) in 1999, he was a Senior Scientist in remote sensing with the System Engineering and Technology Group, Lockheed Martin, NASA Stennis Space Center, where he supported a number of NASA projects, from hyperspectral spaceborne/airborne instrument preflight calibration, inflight radiometric and spectral calibration, and validation and verification to advanced remote sensing applications. He is currently the Chief of the Satellite Calibration and Data Assimilation Branch, NOAA/National Environmental Satellite, Data, and Information Service/Center for Satellite Applications and Research/Satellite Meteorology and Climatology Division, College Park, MD, USA. His work specializes in the calibration of radiometers onboard NOAA's operational environmental satellites. In addition to operational pre- and postcalibration support, he is responsible for developing and refining the methodology for intersatellite calibration using the simultaneous nadir overpass method, which has been used for the long term on orbit instrument performance monitoring of all radiometers on NOAA's polar orbiting satellites, and is being used by scientists for quantifying intersatellite calibration biases in developing long-term time series for climate change detection studies. He has authored or coauthored more than 160 papers in international peer-reviewed journals. His primary research interest is climate quality calibration for earth-observing satellites.

Dr. Cao chaired the Committee on Earth Observation Satellites/Working Group on Calibration/Validation, the international committee for all space agencies, from 2007 to 2008. And in the past several years, he has been leading developments in S-NPP and NOAA-20 VIIRS calibration and validation. He is currently the Co-Chair of the Calibration Product Oversight Panel and the Chair for the GOES-R Calibration Working Group.